applied sciences

MDPI

Article

Analysis of Dual- and Full-Circular Polarimetric SAR Modes for Rice Phenology Monitoring: An Experimental Investigation through Ground-Based Measurements

Yuta Izumi [1,*], Sevket Demirci [2], Mohd Zafri bin Baharuddin [3], Tomoro Watanabe [1] and Josaphat Tetuko Sri Sumantyo [1]

1 Center for Environmental Remote Sensing, Chiba University, Chiba 2638522, Japan; afaa0135@chiba-u.jp (T.W.); jtetukoss@faculty.chiba-u.jp (J.T.S.S.)
2 Electrical and Electronics Faculty of Engineering, Mersin University, Mersin 33343, Turkey; sdemirci@mersin.edu.tr
3 Department of Electronics and Communication Engineering, Tenaga national University, Kajang 43000, Malaysia; zafri@uniten.edu.my
* Correspondence: yutaizumi0927@gmail.com; Tel.: +81-80-1671-9266

Academic Editors: Carlos López-Martínez and Juan Manuel Lopez-Sanchez
Received: 23 February 2017; Accepted: 4 April 2017; Published: 7 April 2017

Abstract: Circularly polarized synthetic aperture radar (CP-SAR) is known to be insensitive to polarization mismatch losses caused by the Faraday rotation effect and antenna misalignment. Additionally, the dual-circular polarimetric (DCP) mode has proven to have more polarimetric information than that of the corresponding mode of linear polarization, i.e., the dual-linear polarimetric (DLP) mode. Owing to these benefits, this paper investigates the feasibility of CP-SAR for rice monitoring. A ground-based CP-radar system was exploited, and C-band anechoic chamber data of a self-cultivated Japanese rice paddy were acquired from germination to ripening stages. Temporal variations of polarimetric observables derived from full-circular polarimetric (FCP) and DCP as well as synthetically generated DLP data are analyzed and assessed with regard to their effectiveness in phenology retrieval. Among different observations, the $H/\bar{\alpha}$ plane and triangle plots obtained by three scattering components (surface, double-bounce, and volume scattering) for both the FCP and DCP modes are confirmed to have reasonable capability in discriminating the relevant intervals of rice growth.

Keywords: radar polarimetry; synthetic aperture radar (SAR); dual circular polarimetry (DCP); compact polarimetry; rice phenology

1. Introduction

Conventional polarimetric synthetic aperture radar (SAR) that adopts linearly polarized (LP) antennas on the transmitter and receiver, aptly named as LP-SAR, has already proven its powerful classification ability. Besides, an important performance consideration involves the technical trade-off between the full-linear polarimetric (FLP) and dual-linear polarimetric (DLP) modes. The FLP mode provides complete polarimetric information which enhances the target parameter retrieval and polarimetric discrimination. However, inherent limitations such as reduction of swath width, an increase of system complexity, data rate, and power consumption will be compromised. DLP systems, on the other hand, overcome these limiting factors but they do not afford complete information regarding the full polarization state of the targets. For example, it results in a less accurate alpha angle parameter [1,2] and does not give the possibility to perform three-component

(surface, double-bounce, and volume scattering) decomposition. In recent years, to circumvent these drawbacks, the idea to use circular polarization or tilted linear polarization in transmission has emerged, so-called compact polarimetric SAR [3–5]. Three modes have been discussed, i.e., the $\pi/4$ mode [4], the dual-circular polarimetric (DCP) mode [5], and the circular transmit while linear receive (CTLR) mode [3]. These different polarimetric SAR modes are categorized as shown in Figure 1.

More recently, a SAR campaign that utilizes circular polarization in both transmission and reception has been proposed (end-to-end circular polarization) and studied for spaceborne and airborne missions [6]. Although this unique circularly polarized SAR (CP-SAR) system requires almost ideal CP-antennas (i.e., 0 dB of the axial ratio (AR)), which may often be difficult to satisfy, recent advances in antenna technologies can acceptably fulfill this requirement (e.g., AR of 1.1 dB is achieved for RISAT-1) [7]. It is also worth noting that the following advantages of CP-SAR usually outweigh this difficulty in antenna requirement. Circular polarization is already known to be less affected by the Faraday rotation which is a significant problem, especially for lower frequency bands (i.e., L and P) [8]. To be specific, the Faraday rotation effect in the ionosphere does not alter the transmitted polarization which is not the case in linear polarization [9]. Less effect of the interference between direct and reflected signals due to multipath propagation is also expected [6]. In addition, being one of the compact polarimetric modes, the DCP mode of CP-SAR yields more abundant polarimetric information than those of the DLP mode. Furthermore, Guo et al. and Zhang et al. highlighted that the DCP mode is the most suitable configuration among compact polarimetric modes to apply the entoropy-alpha ($H/\bar{\alpha}$) decomposition when this decomposition is performed on a 2×2 coherency matrix [10,11]. Despite its usefulness, however, CP-SAR has not been practically exploited in Earth observation, and many studies on compact polarimetry reconstruct the compact data by converting from LP-SAR data (i.e., simulated circular polarization data).

Among polarimetric SAR practices, rice monitoring has been one of the important applications since rice is a staple food for almost half the world's population. A less-explored topic in this field is the rice phenology retrieval from the time-series SAR data. This information is of great importance in planning of cultivation practices, yielding estimation and water management. Various analyses of rice monitoring from polarimetric SAR data have been addressed for this purpose [12–16]. Although the classical LP-SAR is the most commonly utilized tool for this task, current studies have been focusing on the compact SAR modes because of their advantages mentioned above [12,14].

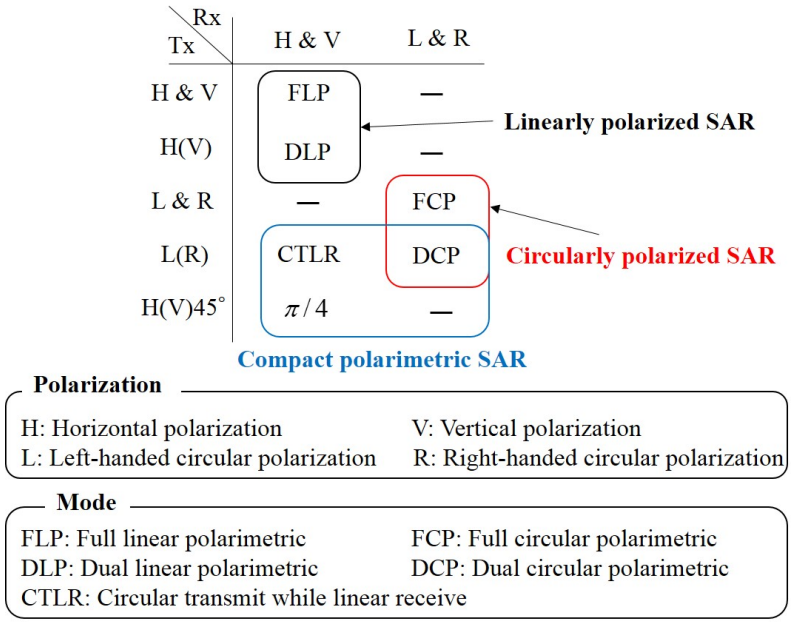

Figure 1. Categorization of various polarimetric synthetic aperture radar (SAR) modes.

Due to the growing interest in the use of circular polarization, we investigate, in this paper, the feasibility of the FCP and DCP modes of CP-SAR and its performance on rice phenology monitoring. For this purpose, a ground-based CP-radar system was adopted, and the time-series C-band backscattering data of a Japanese rice paddy (*Oryza sativa* L.) were analyzed. The rice samples were repeatedly observed within an anechoic chamber from germination to ripening stages. To analyze the radar backscatter as a function of growth stages, different polarimetric signatures and target decomposition techniques are exploited for both FCP and DCP data. In addition, $H/\bar{\alpha}$ decomposition for the DLP mode is also examined for comparison purposes.

The paper is organized as follows: the polarimetric decomposition and analysis methodologies for the FCP, DCP, and DLP modes are demonstrated in the next section. Section 3 provides an explanation of the employed ground-based CP-radar system and its polarimetric calibration, the phenological description of the measured rice samples, and the methodology used in data analysis. The experimental results and discussion are given in Section 4. The last section concludes the paper.

2. Methodology

Since compact polarimetric SAR systems have been gaining increasing attention, the aim of this study is to assess the performance of the DCP mode by comparing its information content with that of the FCP mode in the case of rice backscattering. For this task, it is required to derive and evaluate the compact versions of eigenvalue/eigenvector-based and model-based target decompositions. The relevant scattering decomposition methods for both the FCP and DCP modes are discussed in the following. The DLP version of eigenvalue/eigenvector-based decomposition is also explained to compare the CP-SAR performance with LP-SAR.

2.1. Target Decomposition for FCP Data

Among a substantial number of incoherent decomposition techniques, we chose Cloude–Pottier eigenvector-based $H/\bar{\alpha}$ decomposition (hereafter referred to as $H/\bar{\alpha}$ decomposition) [17] and four-component model-based decomposition for the FCP mode [18,19]. Applying the $H/\bar{\alpha}$ decomposition, the polarimetric entropy H and alpha angle α can be deduced, where H represents scattering randomness, and the α is associated to the corresponding scattering mechanism represented by each eigenvector [17]. The four-component decomposition technique yields four elementary scattering mechanisms, i.e., surface, double-bounce (or dihedral), volume (or multiple), and helix scattering. This methodology was first proposed by Yamaguchi et al. [18], and we adopt herein the improved four-component decomposition proposed by Singh et al. [19] which fully accounts for coherency matrix coefficients.

To apply the aforementioned decomposition theories to FCP data, linear to circular polarization basis transformation is used to obtain first the three-dimensional (3D) Pauli scattering vector in circular basis, given as:

$$\mathbf{k_p} = \frac{1}{\sqrt{2}} \begin{bmatrix} -j2S_{LR} \\ (S_{LL} - S_{RR}) \\ -j\,(S_{LL} - S_{RR}) \end{bmatrix}, \tag{1}$$

where S_{xy} are the elements of the scattering matrix with x and y denoting the received and transmitted waves respectively, and subscripts L and R represent left-handed circular polarization (LHCP) and right-handed circular polarization (RHCP) respectively. The averaged coherency matrix can then be obtained via the Pauli scattering vector in (1) as:

$$\langle [\mathbf{T_{FCP}}] \rangle = \left\langle \mathbf{k}_p \cdot \mathbf{k}_p^{\dagger} \right\rangle, \tag{2}$$

where the superscript † indicates conjugate transpose, and <·> indicates the ensemble averaging operation. This tailored coherency matrix for circular polarization basis makes it possible to adopt decomposition techniques in a similar fashion to linear polarization basis. Under ideal conditions

where there are no adverse effects, the information content of FCP and FLP data are identical because each can be transformed to the other via the unitary matrix.

2.2. Target Decomposition for DCP Data

Recently, several target decomposition theories for compact polarimetric SAR data have also been proposed. There are three main groups, which differ in the type of the symmetry assumptions that they made about the observed media and/or the matrix used in decomposition: decomposition deduced by the Stokes vector [20]; 2×2 coherency matrix [10]; and 3×3 pseudo-coherency matrix [21]. Here, we note that the decomposition deduced from the 3×3 pseudo matrix was not adopted in this study since the assumed relationship between the correlation coefficient and cross-polarization ratio would not always be valid [21]. Thus, we employed two decomposition approaches, one based on the Stokes vector and the other on the 2×2 coherency matrix, which carry identical information [20]. The $H/\bar{\alpha}$ decomposition and the three-component decomposition are explained below.

2.2.1. $H/\bar{\alpha}$ Decomposition

We use the unexpanded 2×2 coherency matrix to implement $H/\bar{\alpha}$ decomposition. With this approach, two eigenvectors corresponding to the first and second dominant eigenvalues can be extracted. The two-dimensional (2D) Pauli vector for circular polarization and the LHCP transmit case is expressed as [10]:

$$\mathbf{k_{DCP}} = \begin{bmatrix} S_{LL} \\ S_{RL} \end{bmatrix}. \tag{3}$$

The coherency matrix is obtained via the Pauli vector in (3) as:

$$\begin{aligned} \langle [\mathbf{T_{DCP}}] \rangle &= \langle \mathbf{k_{DCP}} \cdot \mathbf{k_{DCP}^{\dagger}} \rangle \\ &= \begin{bmatrix} u_1 & u_2 \end{bmatrix} \begin{bmatrix} \lambda_1 & 0 \\ 0 & \lambda_2 \end{bmatrix} \begin{bmatrix} u_1 & u_2 \end{bmatrix}^{\dagger}. \end{aligned} \tag{4}$$

Here, λ_i are the eigenvalues and u_i are the orthogonal eigenvectors of the unitary matrix

$$u_i = e^{j\phi_i} \begin{bmatrix} \cos\alpha_i e^{j\delta_i} & \sin\alpha_i \end{bmatrix}^{\mathrm{T}}, \tag{5}$$

where superscript T denotes the transpose operation. The H and mean α ($\bar{\alpha}$) are then given by:

$$H = \sum_{i=1}^{2} P_i(-\log_2 P_i), \tag{6}$$

$$\bar{\alpha} = \sum_{i=1}^{2} P_i \alpha_i, \tag{7}$$

where scattering probabilities are:

$$P_i = \frac{\lambda_i}{\lambda_1 + \lambda_2} (i = 1, 2). \tag{8}$$

The $\bar{\alpha}$ values for the surface, dipole, and double-bounce scattering mechanisms can be calculated from (4), (5), and (7). The corresponding values are shown below together with the FCP values for comparison.

$$\text{surface (DCP)} : 90^{\circ}, \quad \text{dipole (DCP)} : 45^{\circ}, \quad \text{double (DCP)} : 0^{\circ},$$

$$\text{surface (FCP)} : 0^{\circ}, \quad \text{dipole (FCP)} : 45^{\circ}, \quad \text{double (FCP)} : 90^{\circ}.$$

α values of the DCP mode are shown to have symmetric values to those of the FCP mode about the $\alpha = 45°$. Therefore, DCP α values are obtained as $\alpha' = 90° - \alpha$ for comparison with the FCP mode in the results section.

The obtained pairs of H and $\bar{\alpha}$ values are then plotted on the $H/\bar{\alpha}$ 2D plane with some boundaries to clarify the scattering mechanism and feasible region [17]. We perform the analysis on the $H/\bar{\alpha}$ plane for displaying the polarimetric signatures of each rice growth stage. Besides, the FCP and DCP modes have different $H/\bar{\alpha}$ plane plots because the boundaries of each zone differs [11]. Here, our main purpose is to compare the performances of the two modes, thus, we display the $H/\bar{\alpha}$ plane with $\alpha' = 90° - \alpha$ condition for the DCP case. Figure 2 shows the $H/\bar{\alpha}$ planes with different boundaries for each case.

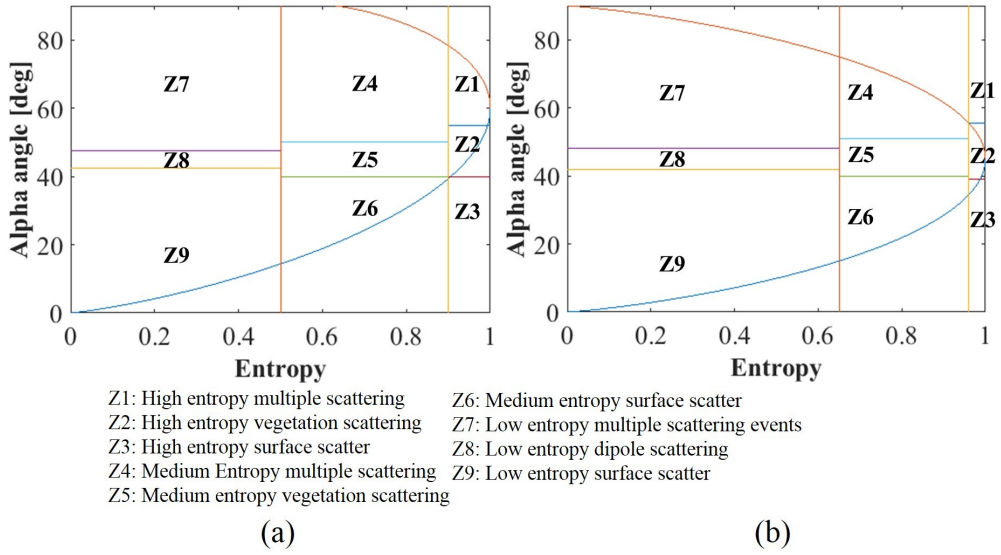

Figure 2. The $H/\bar{\alpha}$ plane. (**a**) FCP and FLP; (**b**) DCP.

2.2.2. Three-Component Decomposition

Cloude et al. proposed compact three-component decomposition theory using the Stokes vector by considering the relation between the Stokes vector and the 3×3 coherency matrix [20]. This method extracts three components; namely, surface, double-bounce, and volume scattering power as a function of dominant α and degree of polarization (DoP) which represents the polarized wave ratio of the total receiving power (similar value with entropy).

The Stokes vector for the DCP mode is defined as (LHCP transmit case):

$$\mathbf{g} = \begin{bmatrix} \langle g_0 \rangle \\ \langle g_1 \rangle \\ \langle g_2 \rangle \\ \langle g_3 \rangle \end{bmatrix} = \begin{bmatrix} \left\langle |S_{RL}|^2 + |S_{LL}|^2 \right\rangle \\ -2Im \langle S_{RL} S_{LL}^* \rangle \\ 2Re \langle S_{RL} S_{LL}^* \rangle \\ \left\langle |S_{RL}|^2 - |S_{LL}|^2 \right\rangle \end{bmatrix}. \tag{9}$$

Three components—the surface (P_s), double-bounce (P_d), and volume (P_v) scattering power—are obtained as:

$$\begin{bmatrix} P_d \\ P_v \\ P_s \end{bmatrix} = \begin{bmatrix} \frac{1}{2} g_0 m (1 - \cos 2\alpha_s) \\ g_0 (1 - m) \\ \frac{1}{2} g_0 m (1 + \cos 2\alpha_s) \end{bmatrix}. \tag{10}$$

where m and α_s represent the DoP and dominant α respectively, defined as:

$$m = \frac{1}{g_0}\sqrt{\sum_{i=1}^{3} g_i^2}, \tag{11}$$

$$\alpha_s = \frac{1}{2}\tan^{-1}\left(\frac{\sqrt{g_1^2 + g_2^2}}{\pm g_3}\right) \quad (+ : \text{LHCP transmit} \quad - : \text{RHCP transmit}). \tag{12}$$

As α_s indicates the dominant α, the same α provided by full polarimetric (FP) data can be recovered only when there is a dominant eigenvector in the coherency matrix of FP and a reflection symmetric medium.

2.3. Target Decomposition for DLP Data (H/$\bar{\alpha}$ Decomposition)

The DLP contains HH/VH or VV/HV scattering matrix coefficients and also yields a 2 × 2 coherency matrix—similar to DCP. Consequently, the $H/\bar{\alpha}$ decomposition approach can be directly performed on this coherency matrix [1,22]. Note that, in this study, we use the synthetically generated DLP data obtained by unitary transformation from circular to linear basis:

$$\begin{bmatrix} S_{HH} & S_{HV} \\ S_{VH} & S_{VV} \end{bmatrix} = 2\begin{bmatrix} 1 & j \\ j & 1 \end{bmatrix}^{-1}\begin{bmatrix} S_{LL} & S_{LR} \\ S_{RL} & S_{RR} \end{bmatrix}\begin{bmatrix} 1 & j \\ j & 1 \end{bmatrix}^{-1}. \tag{13}$$

The coherency matrix is then expressed by the outer product of the Pauli vector in the same manner as given in (4) (H transmit):

$$\mathbf{k_{DLP}} = \begin{bmatrix} S_{HH} \\ S_{VH} \end{bmatrix}, \tag{14}$$

$$\begin{aligned} \langle[\mathbf{C_{DCP}}]\rangle &= \langle \mathbf{k_{DLP}} \cdot \mathbf{k_{DLP}^{\dagger}} \rangle \\ &= [\mathbf{U_2}]\begin{bmatrix} \lambda_1 & 0 \\ 0 & \lambda_2 \end{bmatrix}[\mathbf{U_2}]^{\dagger}, \end{aligned} \tag{15}$$

where $[\mathbf{U_2}]$ is

$$[\mathbf{U_2}] = \begin{bmatrix} \cos\alpha & -\sin\alpha e^{-i\delta} \\ \sin\alpha e^{i\delta} & \cos\alpha \end{bmatrix}. \tag{16}$$

To compute H for the DLP mode, the same equation of the DCP mode given in (6) is used. Calculation of $\bar{\alpha}$, however, requires a different process, given as:

$$\bar{\alpha} = P_1\alpha + P_2\left(\frac{\pi}{2} - \alpha\right), \tag{17}$$

where P_i are calculated in the same manner as (8). Note that the boundary curves of the $H/\bar{\alpha}$ plane for the DLP mode are the same as the DCP curves (see Figure 2b).

3. Experimental Scheme

3.1. System Description

Circular polarization can be achieved by setting a 90° phase difference between H and V polarizations [23]. To introduce this concept, we employed diagonal dual LP-horn antennas with a phase shifter for transmitting and receiving the CP-signal. The vector network analyzer and rotational positioner controlled by the positioner controller were utilized to construct the whole CP-radar system. The experimental geometry illustrated in Figure 3 was adopted, and the rice measurements were conducted within an anechoic chamber to achieve a fully controlled environment. The incidence angle

was set to 70°, and the operational frequency was adjusted to 4.5–7.5 GHz (bandwidth is 3 GHz) in C-band. An angular span of 0° to 359° was used to investigate the rice backscattering from all azimuth angles. Therefore, quasi-monostatic antennas always face the target direction.

Before starting experiments, the measurement of the AR parameter of the antennas was needed in order to check the deviation from circular polarization. Theoretically, 0 dB of AR shows ideal circular polarization whereas an infinite value corresponds to ideal linear polarization [23]. An AR value of less than 3 dB is generally considered as an acceptable value for most applications [24], and we follow this definition in this paper. The AR of our CP-antennas was measured inside the anechoic chamber and was found to be under 2.5 dB over the entire operational frequency bandwidth which means that our antennas achieve good circular polarization purity within the investigated bandwidth.

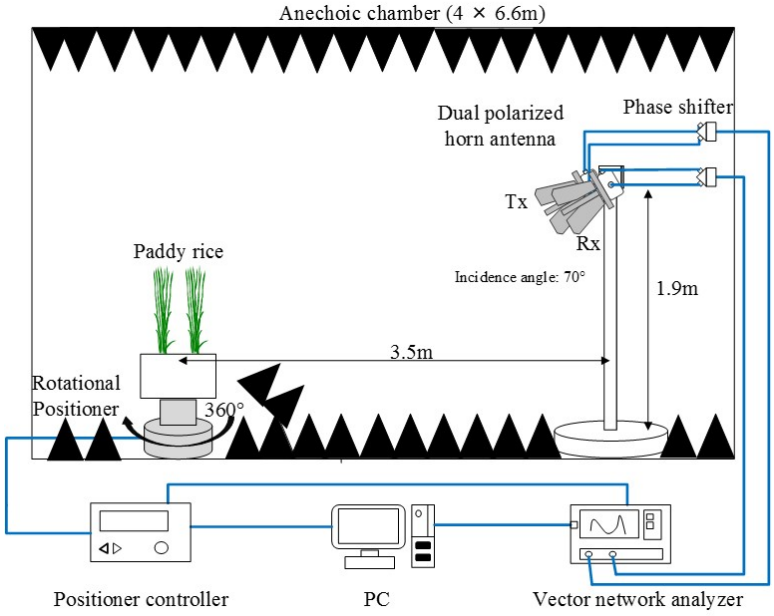

Figure 3. Experimental geometry inside an anechoic chamber.

3.2. Polarimetric Calibration of CP-SAR System

The scattering matrix of all multi-polarimetric radar systems is easily contaminated by system-introduced distortions such as polarimetric channel imbalances, crosstalk, antenna gain, and impurity of polarization. This contamination inevitably degrades the polarimetric decomposition results, and thus polarimetric calibration should be performed in all cases. Here, we introduce the FLP calibration method proposed by Wiesbeck et al. [25] as a suitable and an effective way for calibrating the ground-based LP-radar systems. To apply this method to CP-radar, an error model in circular polarization basis is constructed [26]:

$$\begin{bmatrix} S^m_{LL} & S^m_{LR} \\ S^m_{RL} & S^m_{RR} \end{bmatrix} = \begin{bmatrix} R_{LL} & R_{LR} \\ R_{RL} & R_{RR} \end{bmatrix} \begin{bmatrix} S^c_{LL} & S^c_{LR} \\ S^c_{RL} & S^c_{RR} \end{bmatrix} \begin{bmatrix} T_{LL} & T_{LR} \\ T_{RL} & T_{RR} \end{bmatrix} + \begin{bmatrix} I_{LL} & I_{LR} \\ I_{RL} & I_{RR} \end{bmatrix}. \quad (18)$$

The model includes receive $[\mathbf{R}]$ and transmit $[\mathbf{T}]$ distortion matrices; an isolation distortion matrix $[\mathbf{I}]$; and correct $[\mathbf{S^c}]$ and measured $[\mathbf{S^m}]$ scattering matrices. With using three types of canonical reflectors, namely, *circular plate*, *dihedral*, and 45° *inclined dihedral*, the error coefficients in distortion matrices $[\mathbf{R}]$ and $[\mathbf{T}]$ can be estimated, as explained in detail in our previous study [26]. Empty room calibration is also needed within the steps to extract the isolation distortion matrix $[\mathbf{I}]$, which can be performed easily by measuring a target free scene.

3.3. Phenology Description of Cultivated Rice

Figure 4 shows the photographs and the layout of the rice target used in our experimental validation. A total of eight rice samples were uniformly planted in a rectangular box of dimensions 0.4 × 0.25 × 0.2 m (width × depth × height). The box was made of polystyrene foam for reduction of unwanted echoes and filled with 0.115 m depth of soil and 0.125 m depth of water, as shown in Figure 4b. Thus, the soil was flooded to realize the actual rice field condition. This condition was kept constant throughout the observation period from June to September to collect data that is sensitive only to the rice growth. The non-rice condition was also observed for investigation of the germination stage, where the only flooded soil exists inside the box.

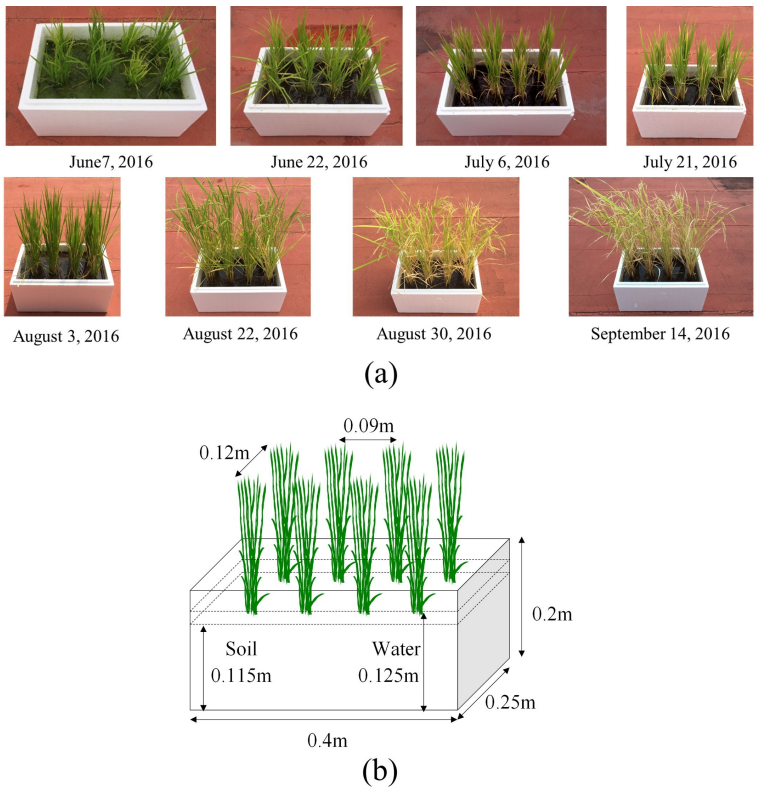

Figure 4. Photographs and layout of the rice used in experimental validation. (**a**) Photographs taken on each measurement date within the observation period from 7 June 2016 until 14 September 2016; (**b**) Layout of the eight rice samples uniformly planted within a container box with 0.115 m depth of soil and 0.125 m depth of water.

To describe the different rice phenological stages, we adopted *Biologische Bundesanstalt, Bundessortenamt und CHemische Industrie* (BBCH) decimal scale [27]. BBCH scale provides the description of actual characteristics of an individual plant such as development rate of leaf, tiller, and panicle [13]. Therefore, utilization of this scale is useful to express rice phenology but not for detail morphological expression. BBCH values for all observed rice conditions are given in Table 1 together with day-of-year (DoY) and mean height as a morphological value. Moreover, based on given BBCH codes, five principal stages were designated, namely, Germination (stage 1), Tillering (stage 2), Stem elongation (stage 3), Booting (stage 4), and Ripening (stage 5) stages, where we referred to [27].

Table 1. BBCH code and phenology stage of each observed data set.

Date	DoY (Day of Year)	Mean Height (cm)	BBCH Code	Phenological Stage
Soil and water	NA	NA	0	1: Germination
7 June 2016	159	19	21-29	2: Tillering
22 June 2016	174	27	21-29	2: Tillering
6 July 2016	188	34	30-39	3: Stem elongation
21 July 2016	203	42	30-39	3: Stem elongation
3 August 2016	216	49	41-49	4: Booting
22 August 2016	235	52	83-85	5: Ripening
30 August 2016	243	52	87-89	5: Ripening
14 September 2016	258	45	93	5: Ripening

Our rice plants were discovered to have an increasing number of tillers until stage 2. Finally, an average of 17 tillers in each stock was observed by 6 July. The increase in the number of tillers was stopped at the end of stage 2 and samples began to initiate panicles inside the stem during stage 3. Just before heading at stage 4, panicles went up and started to come out of the stems. Finally, we found head emergence on 6 August for this type of rice sample.

3.4. Methodology of Data Analysis

As explained in Section 3.1, we adopted a 2D inverse SAR (ISAR) data collection geometry with a fixed incidence angle. Thus, the frequency domain backscatter data of rice samples were acquired for the complete azimuth angles from 0° to 359°. Figure 5 shows the reconstructed images of one sample of data observed on 30 August 2016, for LL, RL, and RR polarizations. A spherical back-projection algorithm is used to process this wide-angle data [28]. From the reflectivity images in Figure 5, it can be clarified that all rice stocks are clearly identified for each polarization thanks to the high-resolution capability of our system. In practical rice monitoring applications, however, the resulted SAR images cannot usually maintain such a high-resolution feature, and a single resolution cell consists of the superposition of different scattering contributions from a few rice plants. Thus, for our situation, all eight rice plants should be confined inside a single resolution cell for a reasonable analysis of rice scattering mechanisms, as Sagues et al. mentioned [29]. For this reason, our analyses are not performed on image data but the scatterometric data obtained by ensemble averaging of the frequency domain data along with all the azimuth angles (0–359°) and frequencies (4.5–7.5 GHz). As a result, the whole scattering behavior is combined into a single coherency matrix as also adopted in [29–31], and the decomposition theories explained in Section 2 are applied to this matrix.

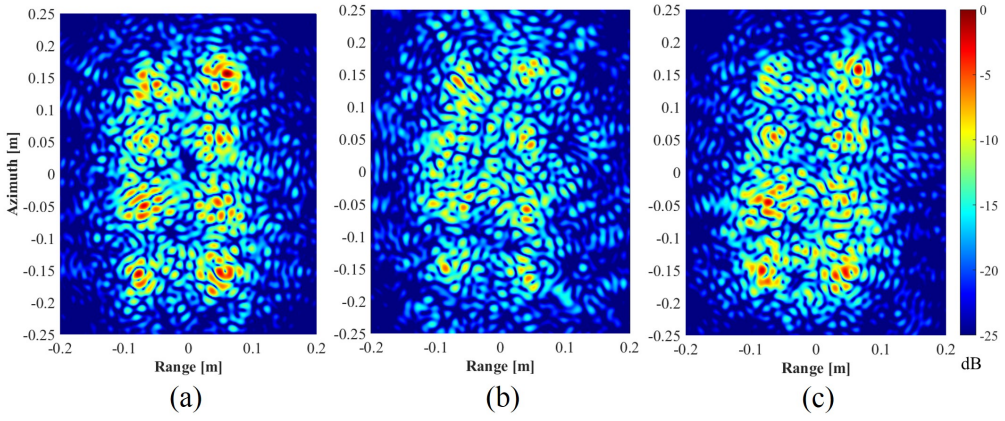

Figure 5. Reconstructed circularly polarized SAR (CP-SAR) images for the rice observed on 30 August 2016. The images are normalized to the maximum value of three images. (**a**) LL polarization; (**b**) RL polarization; (**c**) RR polarization.

4. Rice Monitoring Results and Discussion

In the following subsection, the backscattering coefficients and the polarimetric decomposition results deduced by the averaged single coherency matrix will be presented for the extraction of physical scattering mechanisms of rice growth.

4.1. Backscattering Coefficient

Three scattering matrix data; S_{LL}, S_{RL}, and S_{RR} were collected by assuming $S_{LR} = S_{RL}$ since the reciprocity theorem almost holds true for our quasi-monostatic setup. Figure 6 shows the intensity of backscattering coefficients (LL, RL, and RR) as a function of DoY. The backscattering coefficients are normalized to a maximum value of the whole observation period. From Figure 6, we can see that the backscattering coefficients for all three polarizations increase as rice plants grow until DoY 235 because these are related to the leaf area index, rice freshness, and rice height [32], where our rice plants stop to increase those heights from DoY 235, shown in Table 1. Before rice emergence from the soil (non-rice observation), the backscattering intensity exhibits very low values as a result of the specular reflection from the flooded ground.

The sense of CP-waves is reversed when they are reflected from flat surfaces and smoothly curved spherical reflectors. Therefore, cross- and co-polarization indicate odd- and even-bounce scattering mechanisms respectively. Based on this fact, it is seen from Figure 6 that the surface (cross-polarization) scattering produces relatively higher intensities than the double-bounce (co-polarization) scattering until the end of stage 3 and the opposite is true for later stages. Nevertheless, the maximum difference between polarimetric channels is around 2 dB which is not so significant.

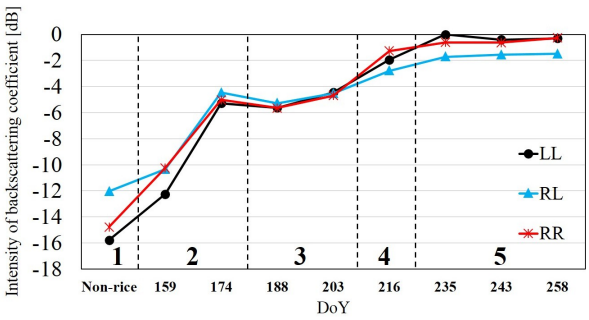

Figure 6. Backscattering coefficients of LL, RL, and RR polarization.

4.2. H/ᾱ Decomposition

The entropy and $\bar{\alpha}$ values for the FCP, DCP, and DLP modes are plotted in Figure 7. Note that the $\bar{\alpha}$ for the DCP mode was treated with the condition $\bar{\alpha}' = 90^\circ - \bar{\alpha}$ for comparison purposes as discussed in Section 2.2.1.

The entropy values shown in Figure 7a exhibit relatively lower values at stage 1, because of the non-planted soil condition which produces highly deterministic scattering. Right after vegetation starts to grow, other scattering mechanisms such as double-bounce and volume scattering make entropy higher. Except for stage 1, entropy values fluctuate within the ranges 0.95–1 for FCP, 0.8–0.9 for DCP, and 0.4–0.6 for the DLP mode. It can also be noted that the entropy values for FCP and DCP represent a similar progressive trend and around 0.12 discrepancy between them. On the other hand, entropy for DLP ranges between 0.4 and 0.6 which is comparably lower than those of FCP and DCP. Furthermore, an abrupt decrease at DoY 203 is also observed in the DLP mode, which is not the case in the FCP and DCP modes.

The $\bar{\alpha}$ characteristic is shown in Figure 7b. FCP and DCP patterns are approximately identical except for non-rice and DoY 159 observations which differ by about $\sim 5^\circ$. Despite this, each pattern shows an increasing trend, indicating a progression from surface scattering to dipole-like scattering.

On the contrary, $\bar{\alpha}$ of DLP reveals a notably different result. Stage 1 measured a high $\bar{\alpha}$ of ~78°, which is regarded as multiple scattering. The value then stabilizes to around ~75° on average.

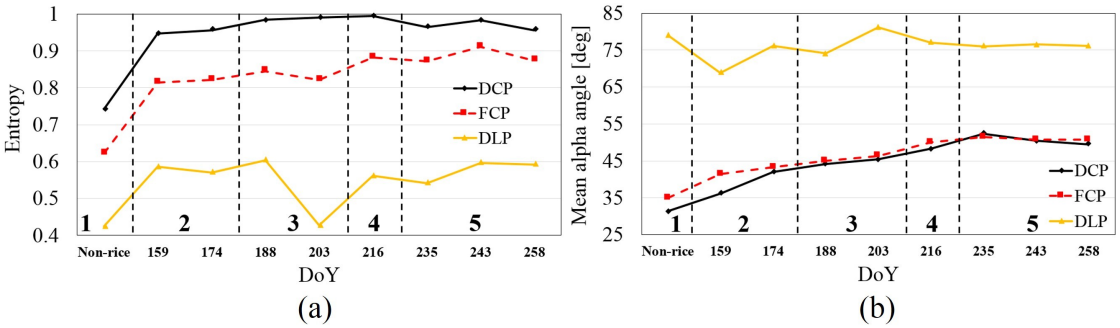

Figure 7. $H/\bar{\alpha}$ decomposition results of the FCP, DCP, and DLP modes. (**a**) Entropy; (**b**) Mean alpha.

To gain a deeper understanding of the scattering mechanisms contained in FCP and DCP data, the independent components of the $H/\bar{\alpha}$ decomposition are investigated separately. Firstly, the appearance probabilities P_i for each scattering type defined by the associated eigenvector are calculated (see (6) and (8) for the DCP case) to interpret the entropy plots in Figure 7a. Note that the decomposition of FCP and DCP data produces three and two eigenvectors/probabilities, respectively. Also, the probability values are constrained by the expressions, $P_1 + P_2 + P_3 = 1$ and $P_1 \geq P_2 \geq P_3$ for FCP, and similarly for DCP. The variation of these probabilities as a function of DoY are displayed in Figure 8. The probability P_1 for DCP data shows a similar trend to that of FCP over the whole observation period but experiences slightly higher value (~10%) for stages 3 and 4. From Figure 8a, an almost constant and relatively large P_3 (recessive scattering) (~10%) is observed for FCP data. This is the case when more than three scattering mechanism components contribute to the receiving signals. Usually, complex targets such as forested areas give rise to this type of multi-scattering. If the third eigenvalue corresponding to P_3 strongly affects the receiving signal, the difference between the entropy values between FCP and DCP becomes higher because entropy is formulated by summation of each independent scattering contribution which corresponds to scattering probability. As Cloude et al. pointed out in [20], compact mode systems typically produce higher entropy compared to the FP system.

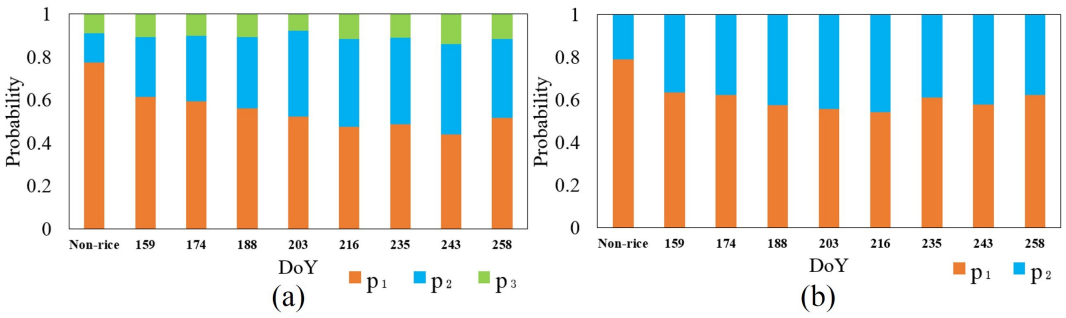

Figure 8. Scattering probabilities for the FCP and DCP modes. (**a**) FCP mode; (**b**) DCP mode.

Secondly, $\bar{\alpha}$ results given in Figure 7b are investigated in terms of their components. For each eigenvector u_i, the corresponding α_i is extracted by using $\alpha_i = \arccos(|u_{1i}|)$ where $|u_{1i}|$ is the absolute value of the first element of the eigenvector. From the results given in Figure 9, we notice that α_1 and α_2 for DCP indicate different trends and values from FCP values. It is observed that α_1 for FCP is close to 45° at stage 4 and fluctuates within the range of 40–65° at stage 5, whereas α_1 for DCP is close to 45° at stage 3 and fluctuates within the range of 60–85° at stages 4 and 5. Thus, these results confirm the necessity of statistical interpretation in terms of $\bar{\alpha}$ values and/or $H/\bar{\alpha}$ space for the discrimination of physical scattering mechanisms.

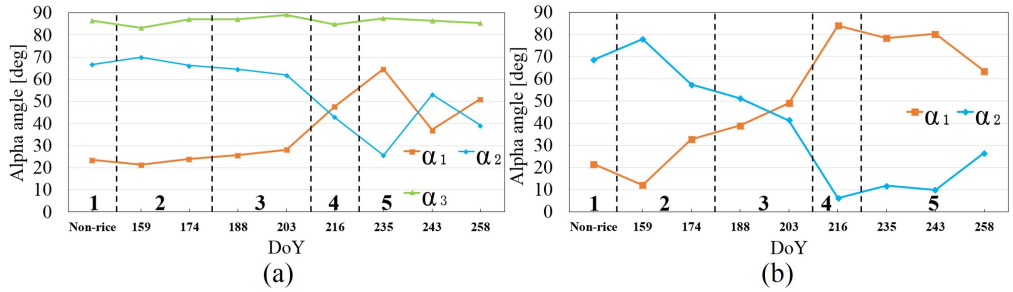

Figure 9. Alpha angle corresponding to each eigenvector. (**a**) FCP mode; (**b**) DCP mode.

Figure 10 displays the $H/\bar{\alpha}$ 2D plane plots obtained from the entropy and $\bar{\alpha}$ values for FCP (Figure 10a), DCP (Figure 10b), and DLP (Figure 10c) measurements. In the FCP mode, the distributions mainly lie in zones 6, 5, and 4, indicating a vegetation-type scattering event. Roughly, four different clusters can be identified: germination stage, tillering stage, stem elongation stage, and booting plus ripening stage, and thus the booting and ripening stages cannot be separated effectively from FCP data. The results for the DCP mode in Figure 10b also reveal a broadened $H/\bar{\alpha}$ pattern, but the two observations (DoY 159 and 174) in the tillering stage are moved away from each other more than the FCP case. Visually, the DCP mode affords better separation between booting and ripening stages compared to the FCP mode, but this cannot be regarded as better capability because the DCP mode has less information content than the FCP mode. Although the $H/\bar{\alpha}$ plane plots for the FCP and DCP modes exhibit some different features, each mode yields satisfactory discrimination of the phenological intervals. In contrast, the $H/\bar{\alpha}$ plane plots for the DLP mode cannot achieve adequate discrimination capability for our rice targets, since almost all intervals are not resolved successfully, as seen from Figure 10c.

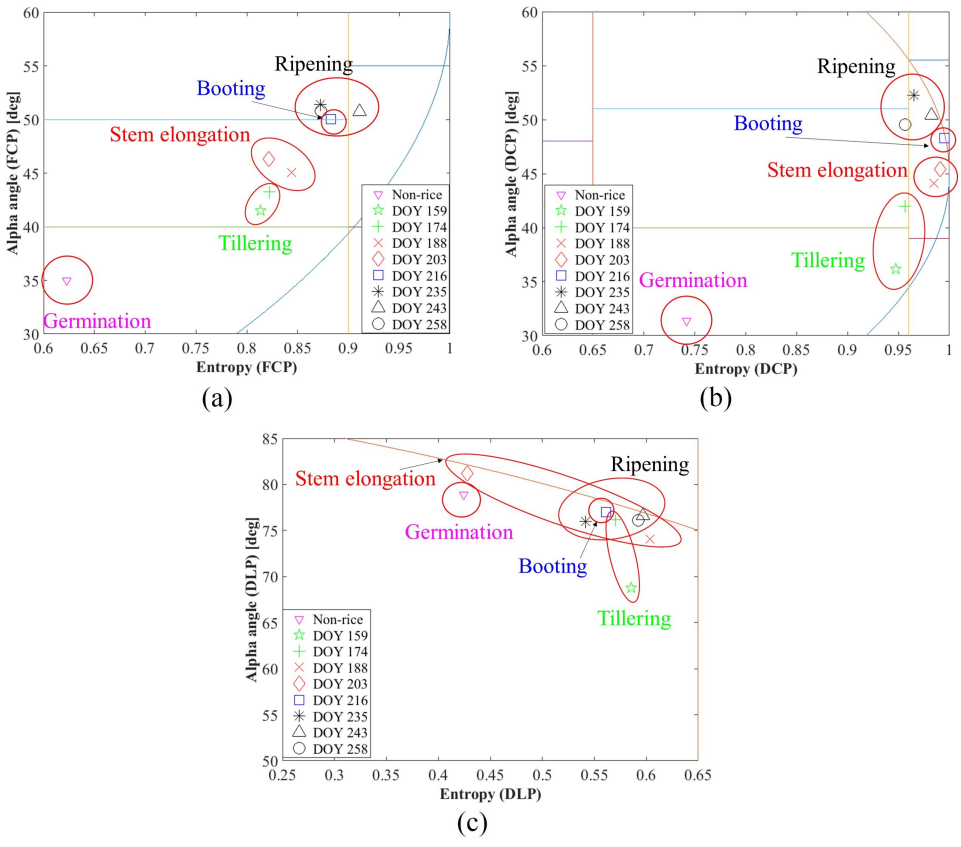

Figure 10. The $H/\bar{\alpha}$ 2D plane. (**a**) FCP mode; (**b**) DCP mode; (**c**) DLP mode.

It is also worth noting that entropy and $\bar{\alpha}$ values for crop backscattering usually increase with increasing incidence angle. For lower incidence angles, surface reflection from soil is dominant whereas, for high incidence angles (e.g., greater than 20°), backscattering from vegetation stems and leaves make dipole-like scattering dominant, as demonstrated in [30]. Therefore, because of our high incidence angle (70°) feature, relatively higher H and $\bar{\alpha}$ values from our experiment than the usual spaceborne SAR incidence angle (common operational mode: <70°) can be expected.

4.3. Four- and Three-Component Decomposition

The four- and three-component decomposition results for the FCP and DCP modes are shown in Figure 11 respectively, where P_s, P_d, P_v, and P_c show surface, double-bounce, volume, and helix scattering respectively. The results are normalized to the maximum value of both modes. In Figure 11a, the double-bounce and surface scattering contributions of four-component decomposition demonstrate a similar evolutionary trend as the backscattering coefficients of co- and cross-polarization in Figure 6. This similarity proves that co- and cross-polarization indicate even and odd bounce scattering mechanisms respectively, as mentioned in Section 4.1. Figure 11a also reveals a stronger volume scattering component than other scattering mechanisms at stages 4 and 5 as well as its evolutionary trend during rice growth. Relatively low helix scattering is also shown, as expected, from vegetation.

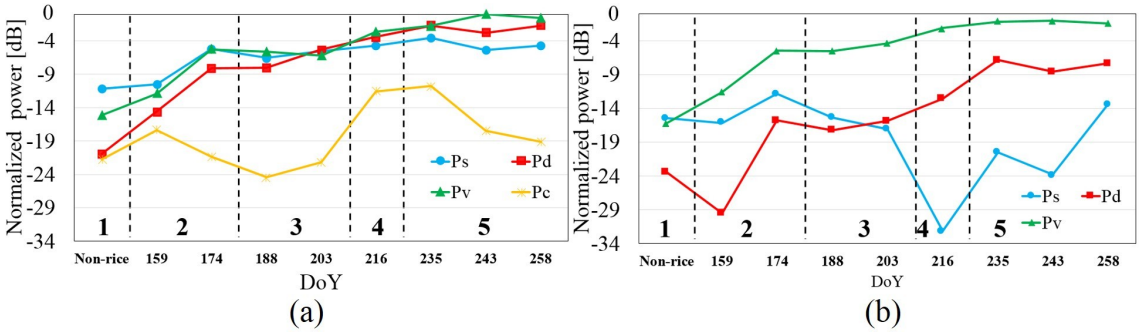

Figure 11. Four-/three-component decomposition results. (**a**) Four-component decomposition results for the FCP mode; (**b**) Three-component decomposition results for the DCP mode.

When we compare the results of both modes, we see that both volume scattering components result in a similar evolutionary trend and value. In contrast, the surface and double-bounce scattering of the DCP mode show lower power than the FCP mode. This error might be attributed to dominant α values because surface and double-bounce scattering are a function of dominant α values, shown in (12). Since we found the dominant α difference between the FCP and DCP modes in Figure 9, this error obviously affects the power level.

To investigate the relative contribution of the scattering component, we present the rate of each scattering mechanism on a triangle plot, which is a similar analysis to [33], shown in Figure 12a,b for the FCP and DCP modes respectively. Note that we exclude the helix scattering contribution from the FCP mode for comparison between both modes. Figure 12a shows similar results to $H/\bar{\alpha}$ display, where the triangle plot for the FCP mode loosely falls into four groups: germination, tillering, stem elongation, and a mix of booting and ripening stages. Therefore, booting and ripening stages still cannot be clearly separated. Moreover, we notice that double-bounce scattering gradually increases as rice grows (from 7% to 36%), while vice versa, the surface scattering decreases in the FCP mode. This situation can also be seen in the DCP mode, where double-bounce scattering increases from 7.8% to 20%, as depicted in Figure 12b. However, as indicated above, the DCP mode shows a relatively stronger volume scattering component (lower surface and double-bounce scattering contribution) in Figure 12b. Therefore, three-component decomposition for the compact mode should be improved to better approximate the FP mode results.

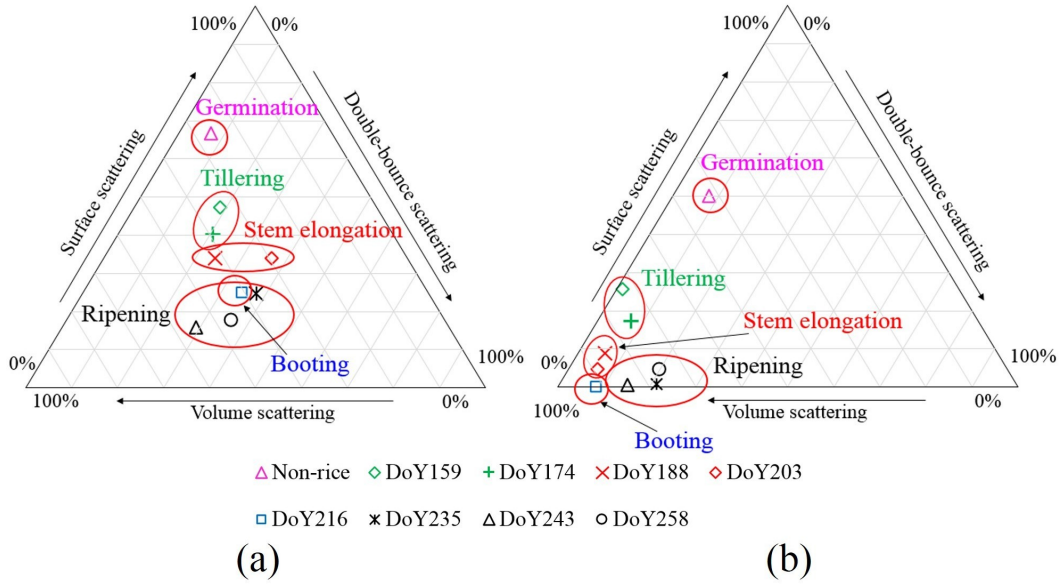

Figure 12. Relative contribution of surface, double-bounce, and volume scattering components on the triangle plot. (**a**) FCP mode; (**b**) DCP mode.

5. Conclusions

This work investigated the FCP and DCP modes of CP-SAR (end-to-end circular polarization system) through rice growth monitoring. For this purpose, self-cultivated rice plants from germination to ripening stages were analyzed by means of frequency domain data measurement using a ground-based CP-radar system. We applied the $H/\bar{\alpha}$ and four-/three-component polarimetric decomposition techniques to measurement data.

The results for the two types of polarimetric decomposition can be summarized as:

- The $H/\bar{\alpha}$ 2D plane showed a satisfactory clear pattern of each stage of rice growth and yielded rough discriminating capability. However, booting and ripening stages could not be separated.
- The DCP mode exhibited better classification capability than DLP mode on the $H/\bar{\alpha}$ 2D plane.
- The four-/three-component decomposition results demonstrated a similar trend of surface and double-bounce scattering as backscattering coefficients of cross- and co-polarization respectively.
- The triangle plot of relative scattering components contribution showed adequate classification capability, similar to the $H/\bar{\alpha}$ plane.

The comparison results between FCP and DCP modes can be stated as:

- Entropy showed a difference of ~0.12 between each other, but overall evolution exhibited similarity. $\bar{\alpha}$ values almost coincided with each other except for non-rice and DoY 159 observations, but dominant and second dominant α resulted in differences.
- The volume scattering component yielded a very similar trend and value. Surface and double-bounce scattering presented different power to each other.

Overall, results for both the FCP and DCP modes of CP-SAR demonstrated adequate rice phenology classification capability. Differences in some polarimetric decomposition parameters between the FCP and DCP modes were noted. Moreover, the DCP mode yielded similar performance to the FCP mode about the $H/\bar{\alpha}$ decomposition and volume scattering, and better classification performance of rice phenology compared to the DLP mode.

This work showed the first results of the ground-based CP radar system for long-term rice observation. We anticipate that this study will contribute to the future development and implementation of CP-SAR systems for space-borne and airborne missions, to be used for precise

and efficient monitoring of vegetation and ground surface by combining the advantages of circular polarization and the compact mode.

Acknowledgments: This work was supported in part by the European Space Agency Earth Observation Category 1 under Grant 6613, by the 4th Japan Aerospace Exploration Agency (JAXA) ALOS Research Announcement under Grant 1024, by the 6th JAXA ALOS Research Announcement under Grant 3170, by the Japanese Government National Budget (Special Budget for Project) FY 2015 under Grant 2101, Taiwan National Space Organization under Grant NSPO-S-105096; Indonesian Bhimasena, and by the Chiba University Strategic Priority Research Promotion Program FY 2016.

Author Contributions: Yuta Izumi led this work. He proposed the idea, processed data, compiled results and wrote this manuscript. Sevket Demirci and Josaphat Tetuko Sri Sumantyo supervised with some fruitful ideas to make this work meaningful. Mohd Zafri bin Baharuddin and Tomoro Watanabe arranged the SAR-system and experiment together with Yuta Izumi.

Conflicts of Interest: The authors declare no conflict of interest.

References

1. Dhar, A.T.; Gray, B.D.; Menges, C.C. Comparison of dual and full polarimetric entropy/alpha decompositions with TerraSAR-X, suitability for use in classification. In Proceedings of the Geoscience and Remote Sensing Symposium (IGARSS), Vancouver, BC, Canada, 24–29 July 2011; pp. 456–458.
2. Sugimoto, M.; Ouchi, K.; Nakamura, Y. On the similarity between dual-and quad-eigenvalue analysis in SAR polarimetry. *Remote Sens. Lett.* **2013**, *4*, 956–964.
3. Raney, R.K. Hybrid-polarity SAR architecture. *IEEE Trans. Geosci. Remote Sens.* **2007**, *45*, 3397–3404.
4. Souyris, J.C.; Imbo, P.; Fjortoft, R.; Mingot, S.; Lee, J.S. Compact polarimetry based on symmetry properties of geophysical media: The $\pi/4$ mode. *IEEE Trans. Geosci. Remote Sens.* **2005**, *43*, 634–646.
5. Stacy, N.; Preiss, M. Compact polarimetric analysis of X-band SAR data. In Proceedings of the European Conference on Synthetic Aperture Radar (EUSAR), Dresden, Germany, 16–18 May 2006.
6. Tetuko, S.S.J.; Koo, V.C.; Lim, T.S.; Kawai, T.; Ebinuma, T.; Izumi, Y.; Baharuddin, M.Z.; Gao, S.; Ito, K. Development of circularly polarized synthetic aperture radar on-board UAV JX-1. *Int. J. Remote Sens.* **2017**, *38*, 1–12.
7. Rao, Y. S.; Meadows, P.; Kumar, V. Evaluation of RISAT-1 compact polarization data for calibration. In Proceedings of the Geoscience and Remote Sensing Symposium (IGARSS), Beijing, China, 10–15 July 2016; pp. 3250–3253.
8. Freeman, A. Calibration of linearly polarized polarimetric SAR data subject to Faraday rotation. *IEEE Trans. Geosci. Remote Sens.* **2004**, *42*, 1617–1624.
9. Souyris, J.C.; Stacy, N.; Ainsworth, T.; Lee, J.S.; Dubois-Fernandez, P. SAR compact polarimetry (CP) for earth observation and planetology: Concept and challenges. In Proceedings of the PolInSAR, Frascati, Italy, 22–26 January 2007.
10. Guo, R.; Liu, Y.B.; Wu, Y.H.; Zhang, S.X.; Xing, M.D.; He, W. Applying *H–α* decomposition to compact polarimetric SAR. *IET Radar Sonar Navig.* **2012**, *6*, 61–70.
11. Zhang, H.; Xie, L.; Wang, C.; Wu, F.; Zhang, B. Investigation of the Capability of *H–α* Decomposition of Compact Polarimetric SAR. *IEEE Geosci. Remote Sens. Lett.* **2014**, *11*, 868–872.
12. Lopez-Sanchez, J.M.; Vicente-Guijalba, F.; Ballester-Berman, J.D.; Cloude, S.R. Polarimetric response of rice fields at C-band: Analysis and phenology retrieval. *IEEE Trans. Geosci. Remote Sens.* **2014**, *52*, 2977–2993.
13. Lopez-Sanchez, J.M.; Cloude, S.R.; Ballester-Berman, J.D. Rice phenology monitoring by means of SAR polarimetry at X-band. *IEEE Trans. Geosci. Remote Sens.* **2012**, *50*, 2695–2709.
14. Yang, Z.; Li, K.; Liu, L.; Shao, Y.; Brisco, B.; Li, W. Rice growth monitoring using simulated compact polarimetric C band SAR. *Radio Sci.* **2014**, *49*, 1300–1315.
15. Hayashi, N.; Sato, M. Measurement and analysis of paddy field by polarimetric GB-SAR. In Proceedings of the Geoscience and Remote Sensing Symposium (IGARSS), Cape Town, South Africa, 12–17 July 2009; pp. IV358–IV361.
16. Li, K.; Brisco, B.; Yun, S.; Touzi, R. Polarimetric decomposition with RADARSAT-2 for rice mapping and monitoring. *Can. J. Remote Sens.* **2012**, *38*, 169–179.
17. Cloude, S.R.; Pottier, E. An entropy based classification scheme for land applications of polarimetric SAR. *IEEE Trans. Geosci. Remote Sens.* **1997**, *35*, 68–78.

18. Yamaguchi, Y.; Moriyama, T.; Ishido, M.; Yamada, H. Four-component scattering model for polarimetric SAR image decomposition. *IEEE Trans. Geos. Remote Sens.* **2005**, *43*, 1699–1706.
19. Singh, G.; Yamaguchi, Y.; Park, S.E. General four-component scattering power decomposition with unitary transformation of coherency matrix. *IEEE Trans. Geosci. Remote Sens.* **2013**, *51*, 3014–3022.
20. Cloude, S.R.; Goodenough, D.G.; Chen, H. Compact decomposition theory. *IEEE Geosci. Remote Sens. Lett.* **2012**, *9*, 28–32.
21. Nord, M.E.; Ainsworth, T.L.; Lee, J.S.; Stacy, N.J. Comparison of compact polarimetric synthetic aperture radar modes. *IEEE Trans. Geosci. Remote Sens.* **2009**, *47*, 174–188.
22. Cloude, S. The dual polarization entropy/alpha decomposition: A PALSAR case study. In Proceedings of the PolInSAR, Frascati, Italy, 22–26 January 2007.
23. Stutzman, W.L. *Polarization in Electromagnetic Systems*; Artech House: Boston, MA, USA; London, UK, 1993.
24. Gao, S.; Luo, Q.; Zhu, F. *Circularly Polarized Antennas*; Wiley: Hoboken, NJ, USA, 2013.
25. Wiesbeck, W.; Kahny, D. Single reference, three target calibration and error correction for monostatic, polarimetric free space measurements. *Proc. IEEE* **1991**, *79*, 1551–1558.
26. Izumi, Y.; Demirci, S.; Baharuddin, M.Z.; Waqar, M.M.; Sumantyo, J.T.S. The development and comparison of two polarimetric calibration techniques for ground-based circularly polarized radar system. *Prog. Electromagn. Res. B* **2017**, *73*, 79–93.
27. Lancashire, P.D.; Bleiholder, H.; Boom, T.V.D.; Langeluddeke, P.; Stauss, R.; Weber, E.; Witzenberger, A. A uniform decimal code for growth stages of crops and weeds. *Ann. Appl. Biol.* **1991**, *119*, 561–601.
28. Demirci, S.; Yigit, E.; Ozdemir, C. Wide-field circular SAR imaging: An empirical assessment of layover effects. *Microw. Opt. Technol. Lett.* **2015**, *57*, 489–497.
29. Sagues, L.; Lopez-Sanchez, J.M.; Fortuny, J.; Fabregas, X.; Broquetas, A.; Sieber, A.J. Indoor experiments on polarimetric SAR interferometry. *IEEE Trans. Geosci. Remote Sens.* **2000**, *38*, 671–684.
30. Lopez-Sanchez, J.M.; Fortuny-Guasch, J.; Cloude, S.R.; Sieber, A.J. Indoor polarimetric radar measurements on vegetation samples at L, S, C and X band. *J. Electromagn. Waves Appl.* **2000**, *14*, 205–231.
31. Zhou, Z.S.; Cloude, S. Structural parameter estimation of australian flora with a ground-based polarimetric radar interferometer. In Proceedings of the Geoscience and Remote Sensing Symposium (IGARSS), Denver, CO, USA, 31 July–4 August 2006; pp. 71–74.
32. Inoue, Y.; Sakaiya, E.; Wang, C. Capability of C-band backscattering coefficients from high-resolution satellite SAR sensors to assess biophysical variables in paddy rice. *Remote Sens. Environ.* **2014**, *140*, 257–266.
33. Yonezawa, C.; Negishi, M.; Azuma, K.; Watanabe, M.; Ishitsuka, N.; Ogawa, S.; Saito, G. Growth monitoring and classification of rice fields using multitemporal RADARSAT-2 full-polarimetric data. *Int. J. Remote Sens.* **2012**, *33*, 5696–5711.